Journal Name

ARTICLE TYPE

Cite this: DOI: 00.0000/xxxxxxxxxx

Computational investigation of carbon based anode materials for Li- and post-Li ion batteries†

Jafar Azizi,*[a] Axel Groß,*[a] and Holger Euchner[b]

Received Date
Accepted Date

DOI: 00.0000/xxxxxxxxxx

Due to its negligible capacity with respect to sodium intercalation, graphite is not suited as anode material for sodium ion batteries. Hard carbon materials, on the other hand, provide reasonably high capacities at low insertion potential, making them a promising anode materials for sodium (and potassium) ion batteries. The particular nanostructure of these functionalized carbon-based materials has been found to be crucially linked to the material performance. However, there is still a lack of understanding with respect to the functional role of structural units, such as defects, for intercalation and storage. To overcome these problems, the intercalation of Li, Na, and K in graphitic model structures with distinct defect configurations has been investigated by density functional theory. The calculations confirm that defects are able to stabilize intercalation of larger alkali metal contents. At the same time, it is shown that a combination of phonon and band structure calculations are able to explain characteristic Raman features typically observed for alkali metal intercalation in hard carbon, furthermore allowing for the quantification of the alkali metal intercalation inbetween the layers of hard carbon anodes.

1 Introduction

Lithium-ion batteries (LIBs) are essential for storing electrical energy, extending from portable electronic devices to e–mobility [1–4]. Due to the foreseeable scarcity of lithium, however, alternative solutions based on more abundant materials have become the subject of contemporary research and investigation. Here, sodium [5] and potassium ion batteries [6] (SIBs and KIBs), frequently categorized as post-Li ion batteries, are the most appealing candidates at the moment. Generally, it has to be pointed out that, with respect to their potential as drop-in replacements for LIBs, there are significant differences in the physicochemical properties of sodium and potassium as compared to lithium. These range from different coordination preferences in compounds to largely varying desolvation energies [7,8]. Hence, finding suitable electrode materials for post-Li ion batteries and understanding their physical and chemical properties is of utmost importance to advance these technologies.

Graphite based materials are still the anode of choice for Li-ion batteries. However, while the lithiation process of graphite results in a succession of binary graphite intercalation compounds (GICs) with a theoretically maxium capacity of 372 mAhg^{-1} for the final LiC_6 stoichiometry, no binary intercalation compounds of graphite with significant sodium content do exist, and hence graphite shows only negligible sodium storage capacity [9]. It has to be noted that this is not simply originating from the larger ionic radius of Na as the even larger K ions have been shown to form GICs. [10–15] In fact, according to theoretical results across all alkali metals (AM), sodium has the weakest chemical binding to a given substrate, indicating that this variation in behavior is not unique to graphite [16].

Consequently, different alternative anode materials have to be considered for NIBs, resulting in hard carbons as promising candidates in particular for Na– and K– ion batteries. The structure of HC is typically described as being composed of differently sized micro- and nano-pores framed by randomly oriented, often curved graphitic domains with large defect concentrations and increased interlayer spacing [17–20]. Carbon atoms within a graphitic layer (of such a domain) are linked by strong covalent bonds, while van der Waals forces are responsible for the interaction between neighbouring layers. Topological defects, which result in the presence of non-hexagonal arrangements of carbon atoms in the graphitic layers, play a crucial role for the diverse morphology and characteristic properties of HCs, as e.g. curved geometries may be explained by their presence [21]. Unlike graphite, which has a d-spacing of 335 pm, the inter-layer spacing of HCs is enhanced and can amount to more than 400 pm which has been proposed to facilitate ion insertion. Especially, synthesis temperature and raw material composition have significant impact on the electrochemical performance of HCs, resulting in a large variation of experimentally observed capacities. For Li-insertion in HC reversible capacities ranging from 210 to 675 mAhg^{-1} [22,23] are reported ,

[a] Institute of Theoretical Chemistry, Ulm University, D-89081 Ulm, Germany
[b] Institute of Physical and Theoretical Chemistry, Tübingen University, 72076 Tübingen, Germany

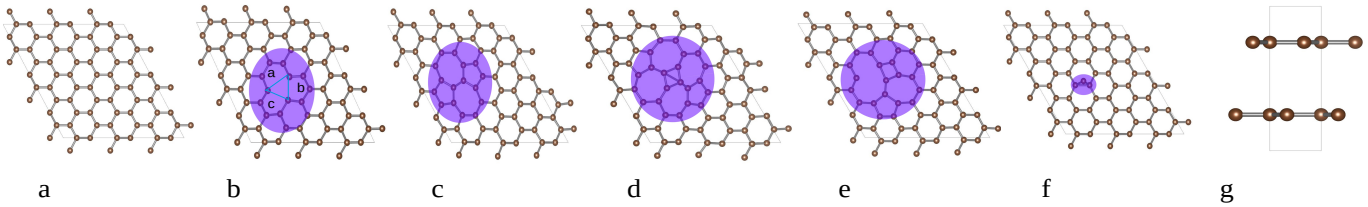

Fig. 1 : Different kinds of defects present in graphite. (a) pristine graphite (b) mono-vacancy (MV) (c) Stone-wales defect (SW) (d) double rotation (DR) (e) mono-vacancy + Stone-wales (MSW) (f) add atom (AA) and (g) side view of the structure used for defect creation.

while in case of Na and K, values from 260 to 640 mAhg^{-1} [24] and 250 to 336 mAhg^{-1} [25–27] have been observed. For instance, when phenolic resin-derived HC is prepared at different temperatures, 1100 °C, 1300 °C, and 1500 °C, the initial reversible capacities for Na intercalation are 337, 358, and 386 mAhg^{-1}, with initial Coulombic efficiencies of 82%, 81%, and 85% , respectively. Similar scenario have been observed for Li and K as well[28].

With respect to the insertion mechanism and structure of the HC, the largely accepted card house model (and modifications thereof) allows for a qualitative description of the processes that underly the observed voltage profil in a charge-discharge curve.[29–32] This model assumes that alkali metal ions are inserted between the layers of graphitic domains in the sloping potential region of the charge-discharge curve,[33–35], whereas the flat low potential region corresponds to the adsorption in micro- and nano-pores, with the potential actually being close to that one of metal deposition.

For the characterization of graphitic materials, often Raman scattering is applied.[31] The main Raman peak that is typically observed is the so-called G-band, which normally appears at about 1580 cm^{-1} and is related to the in-plane motion of the carbon atoms in the graphitic planes. Interestingly, the presence of defects results in the additional observation of the so-called D-band at around 1360 cm^{-1}. However, the D-band does not correspond to a $\Gamma-$point phonon, as is the case for normal Raman modes. Instead, it results from a more intricate inter-valley phenomenon known as double resonance and contains indirect information on the electronic band structure[36,37].

For a knowledge based design of hard carbon anodes, the impact of structural factors such as porosity, carbon binding motifs, and even heteroatom concentration on the functionality of the material must be understood[38–40]. While there have been several theoretical studies regarding defects' role in graphitic systems, defect types, and their functionality have not been thoroughly considered in these investigations.[41–43] Therefore, by investigating the impact of defects on the alkali metal storage mechanisms, we have made a first step towards such an understanding. In this work, the impact of different types of carbon defects on intercalation sites and voltages, vibrational properties and electronic band structure was studied with respect to the intercalation of Li, Na and K. Defects are known to be abundant in HC[17–20]. Furthermore, they strongly interact with metal atoms. Hence the fraction of ions that can be intercalated, especially in the case of Na, increases significantly in the presence of defects. This makes the consideration in the intercalation/adsorption process at defect sites necessary due to their significant role in the AM-ion storage mechanism. While defects obviously do affect the local atomic configuration, it will be demonstrated that the basic features of the band structure and the phonon dispersion curves remain unaffected.

2 Computational Methods

To investigate the impact of different structural motives on the properties of hard carbon, model systems have been studied by density functional theory (DFT). A periodic setup, based on a stacking of two graphitic layers has been chosen to represent the graphitic domains of HC.

Different defect types and the resulting intercalation sites have been investigated in supercells of AMC_{108-x} and AMC_{144-x} stoichiometry. Furthermore, to mimic the Li, Na, and K intercalation process, defect containing GIC model structures with increasing AM content – derived from supercells with AMC_6, AMC_8, AMC_{12}, AMC_{24} and AMC_{48} stoichiometry – have been investigated. All simulations were performed with the Vienna Ab Initio Simulation Package (VASP)[44], using the Projector Augmented Wave(PAW) approach[45]. Exchange and correlation were described via the optPBE functional, which includes a non-local correction scheme to account for van der Waals interactions[46]. Each structure, was optimized with respect to lattice constant and atomic positions, applying a plane wave cutoff of 600 eV. The structures based on the C_{108} supercell was computed with a $4\times4\times4$ k-point mesh, while the other system sizes under investigation were optimized with similar k-point resolution. For the determination of the electronic band structure the number of k-points was doubled. The phonopy code and the finite displacement method were used to determine the vibrational properties. Finally, the resulting phonon dispersion curves and electronic band structures were back-folded to the first BZ of graphite, allowing for a direct comparison along the high-symmetry directions F ($\Gamma-K-M-\Gamma$). For the backfolding of the phonon dispersion curves the Phonon Unfolding code has been used, whereas the bandup code has been applied for the backfolding of the electronic band structure[47–50].

3 Results

3.1 Defect structure

To gain a basic understanding of the morphology and storage mechanism in hard carbon, the impact of different defect motives on the alkali metal insertion has been investigated. For this purpose, defect motives comprising mono-vacancy (MV), Stone-Wales defect (SW), double rotation (DR), add atom (AA), and

a combination of monovacancy and Stone-Wales defect (MSW) have been introduced in the simulation cell. Fig. 1 depicts the defect containing layer of the two layer simulation cell as well as a defect-free graphite sheet for comparison.

The most simple defects in graphitic materials are monovacancies, which are obtained by the removal of a carbon atom. This results in three undercoordinated carbon atoms that are triangularly arranged (see Fig. 1b)) and typically bend out of the graphitic plane. The Stone-Wales (SW) defect is considered to be one of the most important topological defects in graphitic materials. It is created by turning four hexagons into two heptagons and two pentagons, which is achieved by the so-called SW transformation, the rotation of one C-C bond by an angle of 90°, as depicted in Fig. 1c). Furthermore, our model configurations also contain a double rotation (DR) which consists in the transformation of eight hexagons into four heptagons, two pentagons and one tetragon as a result of a 90° rotation of two neighboring C-C bonds. This defect usually causes the bending of the graphene sheets, perpendicular to the line that connects the two pentagons (see Fig. 1d). Moreover, the combination of a MV and SW defect has been constructed (see Fig. 1e)). Joining the structural motivs of these two defects yields a new defect type, consisting of a tetragon, a pentagon, a heptagon, and a decagon. Finally, a carbon adatom placed close to one of the graphitic layers was investigated, and has been found to preferentially adsorb on a bridge site, while adsorption in the center of a hexagon and directly on top of a carbon atom is less favorable. The carbon adatoms thus results in a triangular configuration on top of the graphitic plane, showing a slightly increased C-C bond length of 1.55 Å as compared to the in plane bond length of 1.5 Å.

Interestingly, the introduction of the defects in our model system has been found to result in a stabilization of the AB stacking, such that for the cases of SW, MSW and MV even an AA-stacked starting configuration is not preserved. The defect containing systems transform to an AB stacking, whereas a defect-free system retains the meta-stable AA-stacking. Finally, it has to be noted that the defects result in slight changes in the C-C bond lengths, however, the effect decreases with increasing distance from the defect center. In the case of the adatom, the layers also prefer to be shifted against each other, however, not a full AB stacking is reached. Instead the layers shift such that the adatom is in the center of a hexagon in one layer, while it is covalently bound to two carbon atoms in the other (on top of a C-C bond).

3.1.1 Energetic stability

The probability of finding a certain defect, is largely determined by the energetic penalty going along with the defect formation. Therefore, we have calculated the defect formation energies for the above introduced defect types (see Fig. 2). A defect's formation energy is defined as

$$E_f = E_d - E_p + \mu n \tag{1}$$

where E_d and E_p are the total energy of the defective and defect-free system, respectively. μ is the chemical potential of carbon, which is estimated by the total energy per atom in graphite, multiplied by the number of removed atoms n.

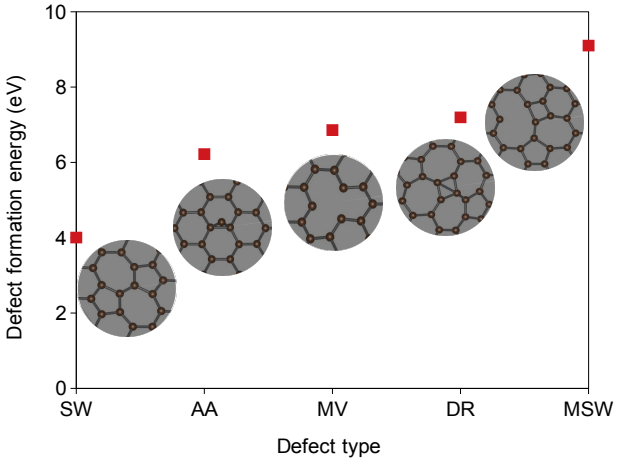

Fig. 2 : Formation energy for the different kinds of defects present in graphite, (a) Stone Wales defect (SW), adatom (AA), mono- vacany (MV), double rotation (DR) and MSW.

The resulting formation energies for MV, SW and AA defect amount to 6.9, 4.0 and 6.2 eV, which is in reasonable agreement with literature (7.3–7.5, 4.5–5.3, and 6.3-8.5 eV for MV, SW and AA respectively) [51–53]. The fact that the here obtained values are slightly lower is likely to be a consequence of different exchange-correlation functionals. While the obtained formation energies clearly show that the SW defect is the most stable of the investigated defect types, the AA is found to be more stable than the MV and the DR (see Fig. 2). Finally, the MSW defect is found to be almost 1.8 eV more stable than the sum of a SW and a MV defect, thus pointing to the reciprocal affinitiy of defects [54]. This is well known for the case of graphite where defect clusters develop during the early stages of melting at elevated temperatures.

Despite the rather high costs for defect formation, precursors and preparation conditions of hard carbon at temperatures typically above 1200 K result in large defect concentrations. Moreover, it has to be noted that defects are often suggested to be one of the reason for the rumpled texture of graphite that is sometimes observed experimentally [55].To elucidate the impact of defects with respect to the use of carbon derivatives as anode material, we have investigated the most favorable intercalation sites for Li, Na, and K in the presence of the simplest defects – MV, SW and AA defect as well as for the case of a MSW defect – and compare it to the intercalation in the defect-free case. For these systems, the energetic stability of a single alkali metal atom at different characteristic positions of the defect structures (see Fig. 4) was investigated by calculating the intercalation energy with respect to the AM–free system:

$$E_{int} = E_{def+ion} - (E_{def} + E_{ion}) \tag{2}$$

Here, $E_{def+ion}$ is the total energy of the graphitic (defect containing) system after the insertion of one AM atom, and E_{def} is the energy of the AM-free layers, wheras E_{ion} is the energy of the AM in the bulk metal phase.

First, the intercalation of an AM ion in defect-free AA and AB

type layers with enforced stacking sequence was investigated for the C_{108} supercell. While the AB stacking (i.e. pristine graphite) is more stable for the ion-free system (by about ≈7 meV/at), the intercalation of one AM ion – corresponding to a AMC_{108} stoichiometry – does result in different scenarios. The intercalation of one Li ion is energetically favorable (see Table. 2), with the AB stacking remaining the more stable configuration. Li is sitting above the center of a hexagon in one layer, while being ontop of a carbon atom for the other. However, already by intercalating one Li atom, the difference in energy between the AA and the AB stacking is reduced to ≈ 4 meV/at. This indicates that further Li intercalation can be expected to result in a stabilization of the AA stacking. For the intercalation of one Na ion, the most stable configuration also corresponds to an AB stacking, however, the Na intercalation is indeed energetically unfavorable, as can be inferred from the positive insertion energy in Table 2. While an AA stacking is found to be less stable, an intermediate stacking involving both AA and AB stacking with the energy almost identical to the AB stacked case was also observed. Finally, for the insertion of one K ion, again the AB stacking is found to be energetically most stable, however, the AA stacking (and an intermediate stacking sequence) is found to be energetically almost degenerate (all within 1 meV/at). Yet, surprisingly, the K intercalation is also found to be energetically largely unfavorable (see Table 2). In contrast to the case of Na, the K intercalation, however, becomes energetically favorable at larger K contents as can be infered from Table 2 for the case of AMC_{48}. Interestingly, for all cases the AB stacking is preserved for low AM concentrations. The reason is that the van der Waals forces between two adjacent layers prevail over the energy gain obtained by the insertion of a low AM fraction. However, the decreasing energy differences between the different stackings already indicate that for larger AM fractions a transition to an AA stacking with the AMs above and below a carbon hexagon can be expected – as is indeed already observed for the case of AM_{48} (see Table 2). This alkali metal concentration is just on the verge of favoring an AA stacking. In fact, in the case of Na and K, the AA stacked configuration is already the more stable one, while for Li the AB stacking is still slightly favored. The observed trend towards an AA stacking corresponds to the sequence of the typical intercalation compounds with increased carbon content, as discussed in literature[56]. Regarding the equivalent situation for the corresponding defect containing systems, clearly shows that the presence of defects can stabilize the insertion of AMs in graphite derivatives, however, the insertion energy strongly depends on the respective intercalation site (see Table 1). Furthermore, as already mentioned above, MV, SW and MSW defects stabilize the AB type stacking, which is then to a large extent also preserved for the low AM contents discussed in the following.

In the case of the MV, the intercalation of a Li ion in one of the three hexagons that get connected by the creation of the MV defect (see Fig. 3a), results in the Li ion moving towards the defect center (position 3), which, as one may have expected, is the energetically most stable site. On the other hand, if a Li atom is placed inside an intact hexagon (position 1, 2, 4, 5 and 6), the atom remains at the center of this site, however, with significantly less energy gain (see Table 1). For Na ions the situation is similar, however, due to their size an off-center position in the hexagonal sites is more favorable due to the interaction with the second layer. As in the case of Li, the site at the defect center is energetically most stable, yielding negative intercalation energies. Here, it has to be noted that two slightly different positions are observed (position 3 and 4), with the Na ion either moving towards an undercoordinated carbon atom or between two such atoms – i.e. the Na ion moves either to a corner or to a side of the indicated triangle. The observed negative intercalation energy clearly shows the stablizing effect of the MV defect for Na intercalation as compared to pristine graphite. Thus, close to the MV defect center, the intercalation of Li and Na is strongly favored, while with increasing distance to this site the insertion energy approaches the situation for defect–free graphitic layers.

For the SW defect, Li atoms move to the center of the created heptagon if they are placed inside the latter one (position 3), whereas placing them on a pentagonal site or a neighboring hexagon results in a shift towards the edges of the pentagon (position 2). Li atoms on hexagonal sites far away from the defect remain centered at these sites (position 1 and 4). Here, again the intercalation in the vicinity of the defect (positions 2 and 3) is found to be the energetically most favorable one (see table 2). Again, for Na the situation is similar, however, the Na intercalation is stable close to the defect (positions 2 and 3), whereas it becomes unfavorable further away. Furthermore, the tendency of the larger Na atoms to shift towards an off-center position remains. The stabilizing impact of the SW defect is found to be smaller than in the case of the MV. This can be attributed to the fact that the graphitic layers do not contain undercoordinated carbon atoms and thus no dangling bonds with unbound electrons that need to be saturated. Instead, in the case of SW defects only the topology is changed, thus having less significant impact on the intercalation process.

The MSW defect is found to result in significant stabilization of Li at the dodecahedral site (positions 1). The heptagonal and the slightly off-centered pentagonal site (positions 2 and 3) are also found to be more stable than the hexagonal site further away from the defect (position 4). For Na the same trend is observed with the dodecahedral site being strongly stabilized. For the above discussed scenarios, the layers keep the AB–stacking sequence after the Li/Na intercalation, meaning that one AM is not enough to induce the transition to an AA stacking in case of a defect being present. While the defect containing layers show no curvature (except DR), they get slightly bent when Li or Na is intercalated. Finally, for the adatom case an intercalated Li moves away from the additional C-C bond. Here, the Li then typically sits close to the center of a top layer hexagon, either on a C-C bond or on top of a C atom (positions 1 and 2), also keeping the AB type stacking. The other situation with Li close to the center of a hexagon and below a carbon atom of the top layer is also possible (position 3), however, energetically significantly less favorable. For Na, the situation is slightly changed. The stacking deviates from AB type with the Na atoms therefore showing a different off-centering. Energetically, however, the Na intercalation remains favorable for these scenarios as well. Due to the large size of K, the inter-

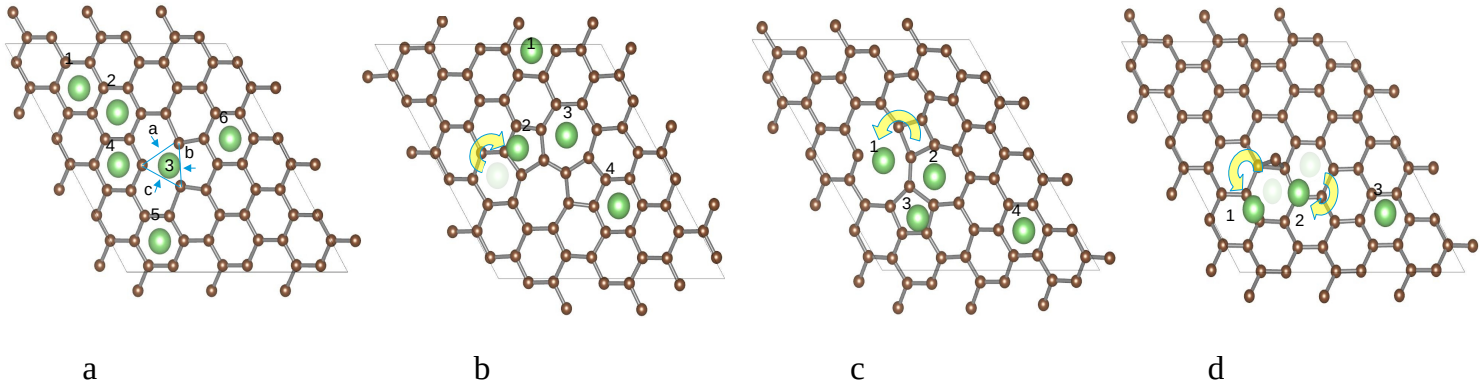

Fig. 3 : Schematic representation of possible Li-intercalation sites for the different model systems (a) MV defect (b) SW defect (c) AA (d) MSW defect. Atoms that have moved to a neighboring site are shown in faint color with an arrow indicating the site they have moved to.

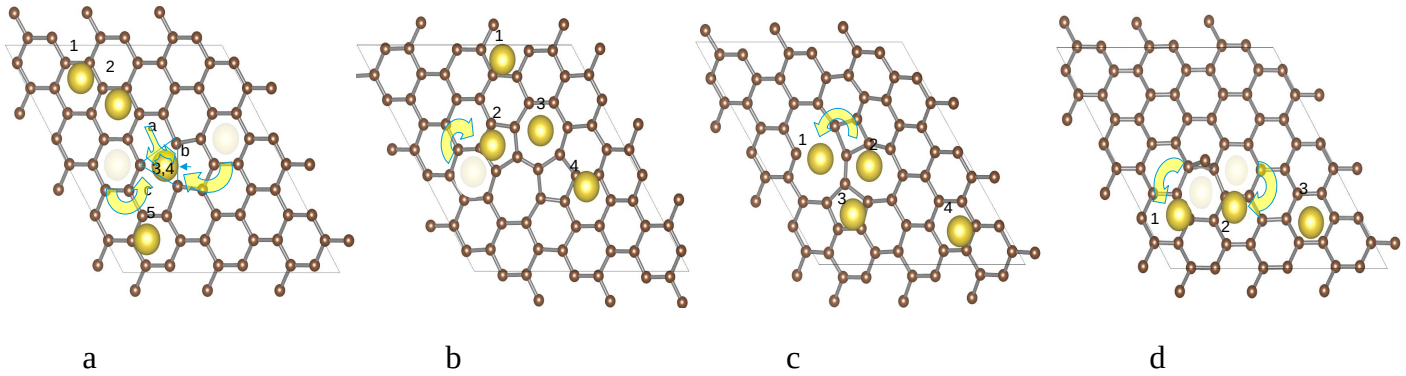

Fig. 4 : Schematic representation of possible Na-intercalation sites for the different model systems (a) MV defect (b) SW defect (c) AA (d) MSW defect. Atoms that have moved to a neighboring site are shown in faint color with an arrow indicating the site they have moved to.

calation process in the defect containing structures is somewhat different. While the presence of defects in principle favors an AB stacking, the K intercalation goes along with a significant increase of the layer spacing and hence reduces the van der Waals interaction between the layers. The structure tries to compensate this by getting more strongly curved in the vicinity of the K ion. Hence, we observe a competition between the attractive van der Waals interaction between the layers and the K insertion. This competition is also present in the case of Na, yet to a much smaller extent, whereas it can almost be neglected for the case of Li. For the MV defect K ions that are further away from the defect move to off-center positions (position 1 and 4), such that they are slighthly off-centered in both the defect containing layer and the defect-free layer sandwiching the ion. Interestingly, these sites are energetically unfavorable as in fact expected from the results for K ions in the defect free system. In the vicinity of the MV defect, the K ion can again occupy the two energetically slightly different sites, either close to the corner or close to the edge of the indicated triangular shape (position 2 and 3). For the SW defect, the K ion in the defect layer prefers either to be close to the heptagon center (position 2) or on top of a C-C bond connecting a penatgon to a hexagon (position 1). In both cases, the K-ion, lies only slightly off-centered with respect to a hexagon in the defect-free layer on top. Energetically, both scenarios result in a slight stabilization of the intercalation process as compared to sites far from the defect. Moreover, it is worth noting that a K ion on the heptagonal site, results in a reduced curvature of the layers. For the MSW case the K ion is found on the sides of the decagon shaped defect (positions 1 and 2), close to an undercoordinated carbon atom. Again the K ion prefers a slightly off-centered position with respect to a hexagon center in the adjacent defect-free layer. This results in a stabilization of the intercalation as compared to the defect free case, with position 1 being energetically more favorable. Finally, the K-intercalation in the vicinity of the adatom results in the K-ion moving away from the C-C bond. This clearly indicates the impact of the ion size. Energetically, positions 1 and 2 become more favorable, whereas an intercalation on position 3 is observed to result in a positive intercalation energy.

In addition, the AM insertion in the larger, C_{144} based, supercells was investigated. The resulting insertion energies showed qualitatively the same trends as for the C_{108} based calculations. In particular, the most stable sites were typically found to differ only slightly in position and energy, which can be understood as a consequence of the small differences in AM and defect concentration (see Table S1 in the SI).

To summarize, the comparsion with the defect-free system (Table 2) makes it clear that only defects are able to stabilize the intercalation of Na and K in the C_{108} based system, whereas Li can stablely be intercalated in AB stacked defect-free graphite. It

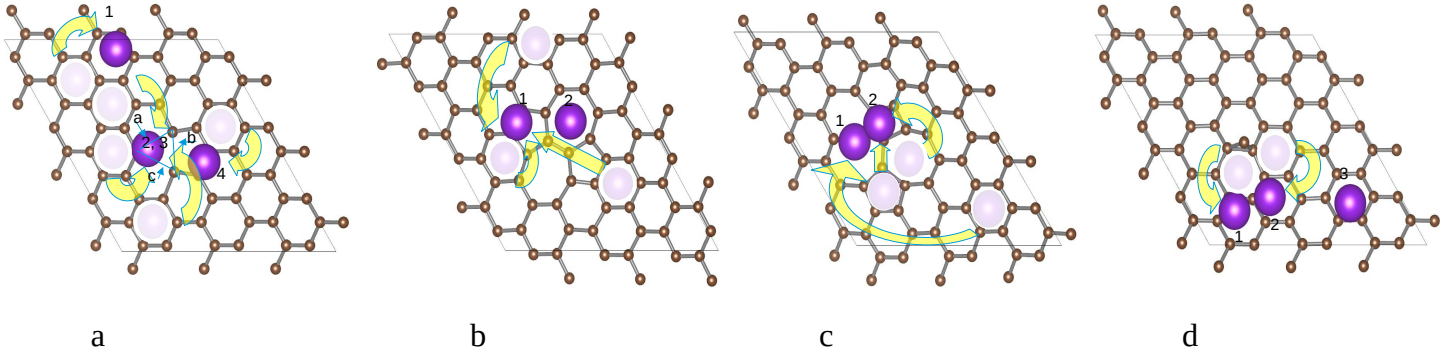

Fig. 5 : Schematic representation of possible K-intercalation sites for the different model systems (a) MV defect (b) SW defect (c) AA (d) MSW defect. Atoms that have moved to a neighboring site are shown in faint color with an arrow indicating the site they have moved to.

Table 1 : Intercalation energy E_{int} (in eV) for Li, Na and K ions at the different sites indicated in Fig. 3, 4 and 5, obtained for the C_{108-x} model system. Note that empty fields (-) indicate that an atom placed at this position moved to a nearby site.

Sites	1	2	3	4	5	6
Li_{mv}	-0.48	-0.53	-1.45	-0.53	-0.53	-0.53
Na_{mv}	0.23	0.18	-0.54	-0.54	0.18	–
K_{mv}	0.38	-0.29	-0.33	0.35	–	–
Li_{sw}	-0.34	-0.56	-0.59	-0.40	–	–
Na_{sw}	0.30	-0.00	-0.00	0.17	–	–
K_{sw}	-0.06	-0.00	–	–	–	–
Li_{msw}	-1.63	-0.79	-0.66	-0.52	–	–
Na_{msw}	-0.79	-0.17	0.08	0.25	–	–
K_{msw}	-0.26	-0.19	–	–	–	–
Li_{aa}	-1.01	-1.02	-0.51	–	–	–
Na_{aa}	-0.45	-0.49	-0.30	–	–	–
K_{aa}	-0.29	-0.34	0.03	–	–	–

Table 2 : Intercalation energy E_{int} (in eV) for Li, Na and K ions regarding AA and AB stacked graphite, for the C_{108} and C_{48} model systems. The energy difference between AA and AB stacked graphite corresponds to E_{AB}-E_{AA}=-0.79 and -0.35 eV for C_{108} and C_{48}, respectively.

Types	Li	Na	K
C_{48-AA}	-0.14	0.39	0.17
C_{48-AB}	-0.15	0.40	0.15
C_{108-AA}	0.23	0.89	1.33
C_{108-AB}	-0.23	0.59	1.11

has to be pointed out that neither Na nor K can stablely be intercalated at low concentrations when no defects are present. This is at first glance suprising as K is known to form K-GICs up to at least KC_8 stoichiometry. This can, however, again be understood as consequence of the competition between interlayer van der Waals interactions and colvalent AM-C bonds. Therefore K-intercalation is only stable at higher K-concentrations within one layer, since then the gain in energy due to the K-C bonds overcomes the energy penalty of reducing the van der Waals interaction due to an increased layer spacing. This is also the reason why Li-GiCs and K-GICs follow different intercalation schemes for dilute AM concentrations.[6] On the other hand, this actually indicates that defects may reduce the overpotential needed to intercalate K in carbon based materials. With respect to the most stable intercalation sites at low AM concentrations, it can be concluded that the exact position and insertion energy depend on an interplay between defect concentration, interlayer interaction and AM ion type.

Finally, it has to noticed that putting the intercalant in the vicinity of a defect site typically results in changes of the C-C bond lengths in the neighbourhood. The observed changes depend on the ion size, such that the strongest curvature and the largest C-C bond change are observed for K-ion intercalation.
After assessing the impact of defects on the intercalation strength with respect to single ions, intercalation compounds with larger fractions of AMs have been investigated. For this purpose, the intercalation process of Li, Na and K in pristine graphite, and two defect-containing systems (MV and SW defect) have been studied. To understand the impact of the different defects on the whole intercalation process and the potential use as anode material the corresponding discharge curves have been determined for a series of AMC_x stoichiometries. The selected systems were filled with increasing AM contents and analyzed with respect to their respective stability. For the phases that were found to be stable at a given AM concentration, the open circuit voltages (OCV) with respect to the pure metal anodes have been determined via the following equation[57]:

$$V_{OCV} = E_{x+1} - (E_x + E_{AM})/z \,, \tag{3}$$

where x is the ion content and z corresponds to the elementary charges that are transferred during the intercalation process. The obtained voltages for the defect-free system as well as for MV and SW defects for Li, Na and K intercalation are depicted in Fig. 6. While the voltage for Li and K remains positive in the presence of the defect for all considered stoichiometries, it becomes negative for Na at higher stoichiometry, indicating that the system has become unstable, i.e. meaning that the intercalation limit is reached. However, unlike in a defect-free system, where Na intercalation is unfavorable already for tiny amounts of Na, in the defective system it becomes at least stable for low ion concentrations.

With respect to the intercalation process, it has to be noted that the interlayer spacing is strongly changed when different AMs are intercalated. This is best seen when comparing (hypothetical) defect–free KC_6, NaC_6, and LiC_6 model structures. The layer spacing for KC_6 amounts to $\approx$ 5.06 Å which is about 13 % larger than for the case of Na and even more than 38 % larger as compared to the interclation of Li. Due to the large differences in ionic radii (Li^+ (0.76 Å) < Na^+ (1.02 Å) < K^+ (1.38Å)), the increased volume for Na and K intercalation compounds is, however, not

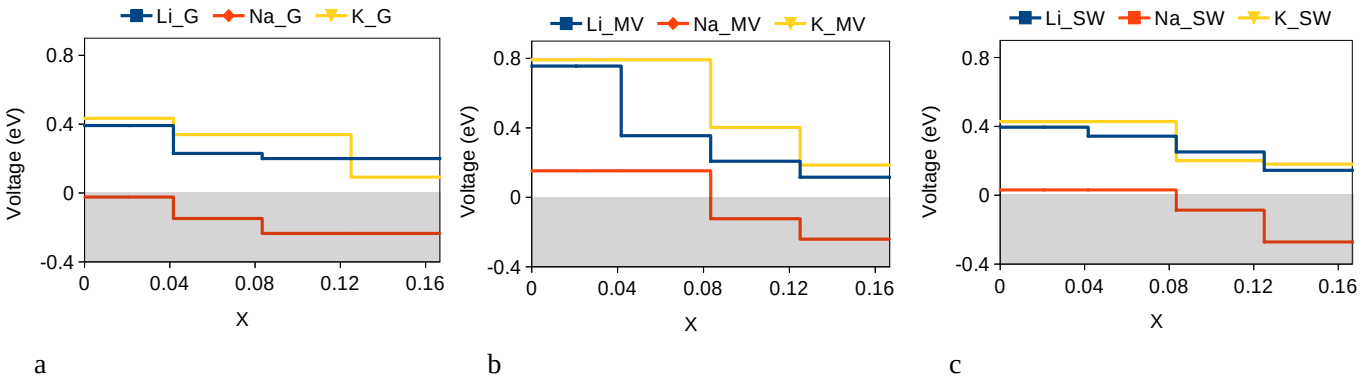

Fig. 6 : Charge/Discharge curves for Li, Na and K intercalation with respect to defect free graphite (G), as well as for model systems containing MV and SW defects calculated in the C_{144-x} model systems. X denotes the concentration of intercalated ions in the investigated model systems (X corresponds to the number of intercalated ions devided by the total number of atoms). The shaded area illustrates that in this part intercalation is energetically unfavorable.

surprising.[58]. As already discussed, for the defect-free system at AM contents close to AMC_{48} stoichiometry a change from AB to AA stacked layers is becoming more favorable. Note that in the following discussion the denoted stoichiometries in case of the MV defect neglect the removed carbon atom. For the MV defect, the AB layer stacking is observed to be favorable up to an AMC_{24} stoichiometry. For AM concentrations corresponding to LiC_{12} and NaC_{12} an AA layer stacking is observed, while for the case of KC_{12} a configuration with intermediate stacking (between AA and AB stacking) is found to be the most stable arrangement. Finally, for the case of AMC_6 Li and Na remain AA stacked and also the K-intercalation comnpounds are approaching this ordering. The situation is similar for the SW defect. As the AM ion concentration increases to AMC_{24}, the AB stacking shifts towards an AA stacking, adapting intermediate configurations. However, when the AM concentration rises to AMC_{12} and higher, the AA stacking becomes more favorable for all ions, while the exact concentration at which the transition takes place is expected to be ion specific. In comparison to the case of a MV defect, the transition to an AA stacking starts earlier in the case of the SW defect. This can be understood with the SW defect system being structurally closer to pristine defect-free graphite, where the transition was already found close to AMC_{48}.

Thus, as already expected from the single ion intercalation, defects enable the intercalation of larger fractions of AMs. However, this comes also along with higher intercalation voltages as can best be seen when comparing the MV and graphite system. While defects thus result in additional capacity in the graphitic layers it also becomes clear that a large part of the AMs that are stored at low potential in hard carbon are not intercalated in the layers but fill micro and nanopores, in agreement with the current picture of AM insertion in hard carbon [31,32,57]. On the other hand it has to be pointed out that the intercalation increases the layer spacing and thus allows for better diffusion through the structure. Therefore, while the additional capacity may partially be due to strongly bound AMs that are responsible for the typically observed irreversible capacity loss during the first charge, the increased number of intercalated AM ions can still be expected to positively affect the kinetics of the material.

3.1.2 Phonon dispersion curves – the G-band shift.

Raman scattering is a frequently used tool for characterizing graphitic structures, yielding a prominent peak at a frequency of ≈ 1580 cm^{-1}, typically referred to as G-band. This peak corresponds to the creation/annihilation of a optical phonon with zero wave vector. Recent works have shown that the alkali metal intercalation in graphitic systems results in a frequency shift of this G-band to lower frequencies[31,32]. Before investigating the impact of the intercalation process, the effect of structural changes in the ion-free system has been studied. For this purpose the dispersion curves of pristine and curved graphite as well as for the case of MV and SW defects have been determined and were backfolded on the high-symmetry directions of graphite – following the reciprocal space direction $\Gamma - K - M - \Gamma$ (see Fig. 7). From a qualitative point of view, the dispersion curves of these four system do not show significant differences, thus pointing to a rather small impact of these structural modifications. This interpretation is confirmed when the G-band positions are extracted. Indeed, here only small variations with a maxium difference of 15 cm^{-1} are observed (see Fig. 7)). Nevertheless, this indicates that increased defect concentrations are expected to result in a slightly increased G-band shift.

As a next step, the vibrational properties of MV and SW defect have been investigated with respect to different AM contents. For this purpose the dispersion curves have again been backfolded on the high-symmetry direction $\Gamma - K - M - \Gamma$ as depicted in (see Fig. 8 as well as Fig. S1 and Fig. S2 in the SI). In addition, the G-band position for the two defect-containing systems has been extracted and compared to the defect-free case. Indeed, for both defect types, as well as for the defect-free system, the phonon dispersion curves show a clear red shift of the G-band for AM intercalation. This means that while defects affect the structure locally, the characteristics of the inplane carbon-carbon bonds, as probed by Raman scattering, are only slightly affected. Furthermore, for low intercalation contents Li, Na and K exhibit only slight differences in G-band position for all scenarios (see Fig. 8 also Fig. S1 and Fig. S2 in the SI). However, by increasing the intercalation content, differences between the ion types are observed, resulting in the strongest G-band shift for Na and the weakest for Li at high AM concentration. This trend is observed for MV and SW

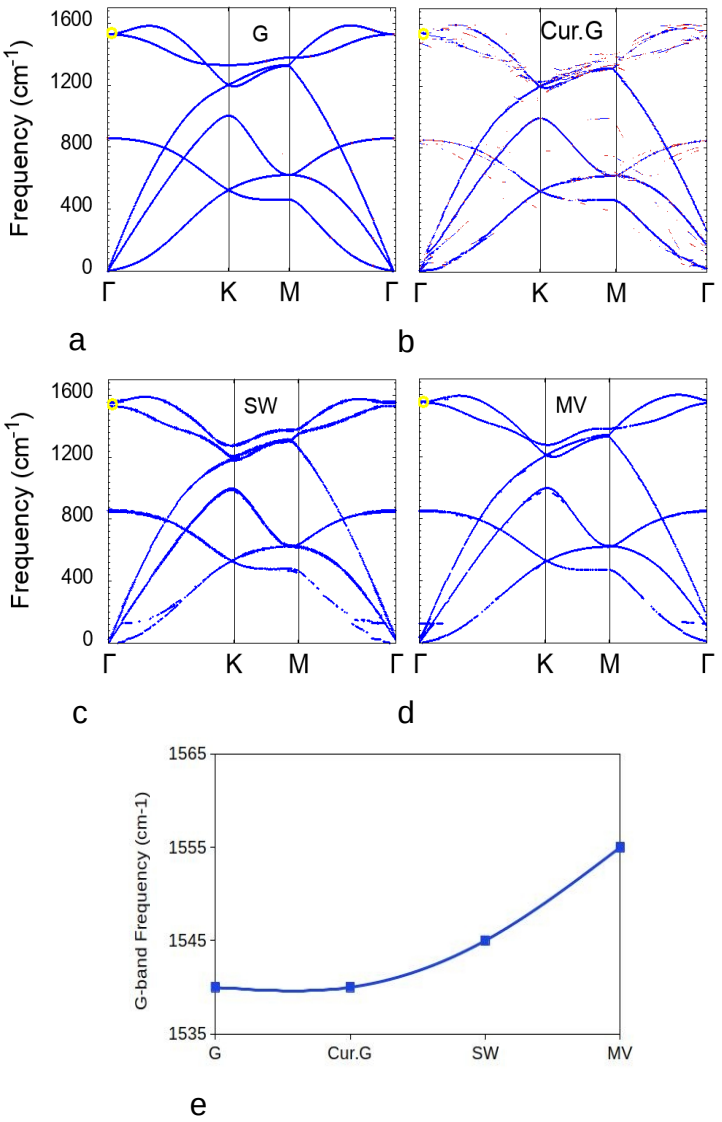

Fig. 7 : Back-folded phonon dispersion curves for Li, Na, and K ions regarding MV defect, as determined by DFT, are shown on the left, center, and right, respectively. Orange circles, represent the predicted positions of phonons that contribute to the G-band

defect as well as for the defect-free system. Surprisingly, the observed order does not correlate with the AM ionic radii and the corresponding lattice spacing. In fact, the G-band vibrations correspond to the inplane motion of the carbon atoms with the akali metal ions not participating in these motions. The different ion sizes and corresponding lattice spacings as well as their electronic structure result in differences in the charge transfer between the alkali metal species and the graphitic planes. These in turn are responsible for differences in the in-plane force constants, which cause the G-band shift.

On a qualitative level, the amount of intercalated alkali metal ions is found to correlate with a decrease of the G-band frequency. In fact, the absolute G-band shift may even be utilized to determine the total number of intercalated ions, with distinct intercalation limits and G-band minima for Li, Na, and K, thus offering a simple and effective way to quantify the degree of intercalation.

3.1.3 Electronic structure.

Apart from the just discussed G-band there is an addtional and rather unique feature in the Raman spectra of graphitic materials, the D-band. This Raman peak is, however, not a Γ-point phonon but is caused by a so-called double resonance Raman (DRR) process.[32] The availability of empty states in the band structure, particularly in the vicinity of the high symmetry points K and $K^{'}$, is a requirement for the occurrence of a DRR process and, consequently, the D-band. In such a process, an excited electron, a non-Γ-point phonon, and a structural defect are involved. First, the wave length of the Raman laser needs to be able to excit an electron to an empty state in the conduction band (see Fig. 10). Before being backscattered by a lattice defect, the excited electron interacts with the crystal lattice resulting in the creation (annhilation) of a phonon. The electron then recombines with the hole it created in the valence band and releases a photon with a longer (shorter) wavelength as a result of energy transfer to (from) the created (annihilated) phonon. It has to be noted that the graphite band structure displays the well-known Dirac cones at the high symmetry points of the Brillouin zone (at K and $K^{'}$), thus enabling the occurence of the DRR process. In conclusion, DRR processes allow probing phonons distant from the center of the Brillouin zone, whereas first order Raman scattering is a technique for the research of phonons close to the G-point. As a result, DRR events provide insight beyond what is accessible by conventional Raman processes, even allowing to extract information on the electronic band structure.

To investigate correlations between AM intercalation and D-band occurence, the electronic band structure was determined and also back-folded on the high-symmetry directions of the first Brillouin zone of graphite. This allows an analysis of our model compounds in a comparative manner. The obtained band structures nicely show the effect of alkali metal intercalation in pristine graphite and for both defect type, as depicted for the case of Na in Fig. 11 (for Li and K see Fig. S3 and Fig. S4 in the SI).

As can be inferred from the band structure, the alkali metal atoms contribute their valence electrons to the system, essentially filling free states of the graphitic band structure (corresponding to a rigid band model like picture). The filling of these states then cause an upshift of the Fermi level. Thus, when the amount of alkali metals increases, the Fermi level continuously shifts upwards, which leads to a lack of free states in the conduction band, thus finally hindering the occurence of a double resonance, corresponding to the experimentally observed disappearing D-band[31,32]. This is indicated by the red arrows in Fig. 11 (see also Fig. S3 and Fig. S4 in the SI), which show the states in the vicinity of the K–point that could be reached by a typical Raman laser of wavelength 633 nm. Note that the length of the arrow corresponds to the energy of such a laser. The analysis of the back-folded band structures reveals that for sodium and potassium compounds with AM contents beyond AMC_{12} no states are accessible above the Fermi, whereas the lithium compounds still offer free states beyond that concentration. This in-

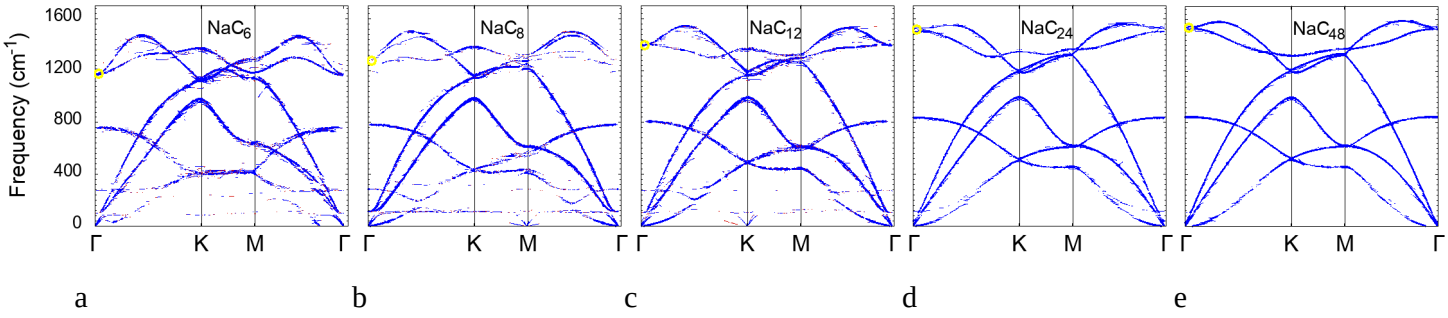

Fig. 8 : Back-folded phonon dispersion curves for Li, Na, and K ions regarding MV defect, as determined by DFT, are shown on the left, center, and right, respectively. Orange circles, represent the predicted positions of phonons that contribute to the G-band

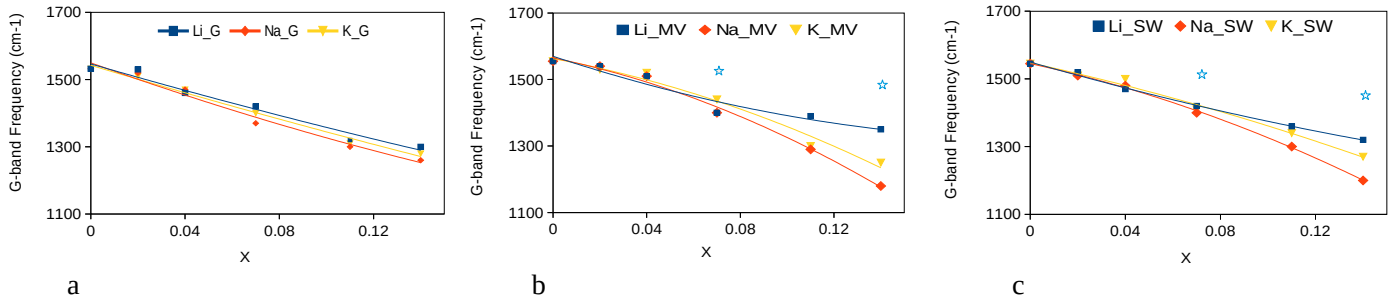

Fig. 9 : G-band shift for Li, Na and K ions regarding defect free graphite (G), MV and SW defects, with X the concentration of AM ions in the C_{144-x} model system (X corresponds to the number of ions devided by the total number of atoms). Note that, the points marked with a star are computed for the C_{108-x} system and therefore correspond to a slightly higher defect concentration.

dicates that while DRR processes are no longer permitted for Na and K, they are still possible for Li. Hence, the D-band is expected to disappear for lower AM concentrations in the case of Na and K. This trend is similar for the MV and the SW defect as well as for the defect-free system, with the Fermi level shifting a bit slower for the MV case, which is due to the filling of missing electrons in the defect site. The overall rather small differencea, however, indicate that the band structure is only slightly affected by the presence of defects. Observable changes with respect to the ion types on the other hand again emphasize differences in the charge transfer. To better quantify the differences in the band structure, the shift in Fermi level as a function of the number of intercalated ions was extracted and depicted in Fig. 12. For all three cases (pristine, MV and SW) the graphs show two distinct regimes for the Fermi level shift. First there is an almost perfectly linear shift of the Fermi level with respect to the number of intercalated ions. This behaviour is observed as long as the intercalation corresponds to the filling of one layer, with the other one remaining empty. This indeed corresponds to a rigid-band like model with the band structure being gradually filled by the additional electrons. Interestingly, the different slopes for Li, Na and K also point to differences in the charge transfer mechanism. When the AM content increases and the second layer is filled the band structure is, in particular for Na and K intercalation, more significantly changed, thus not fulfilling the same linear scaling any more. In fact, for all Li contents, we detect degenerate bands for the Dirac cone at the K-point, whereas for Na and K ions, except for high contents, a splitting is shown. This splitting is a consequence of the increased ion size of Na and K, which results in different layer spacings between empty and ion-containing layers. This can nicely be shown by investigating ion-free structures

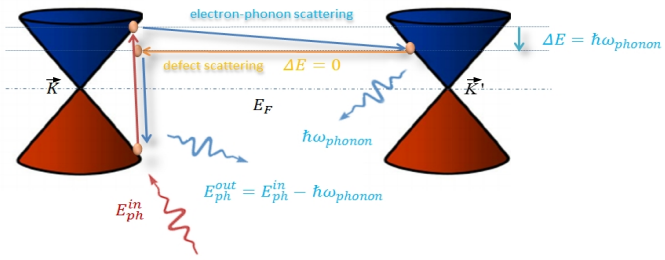

Fig. 10 : A double resonance process is illustrated schematically with respect to the electronic band structure near the highsymmetry points.

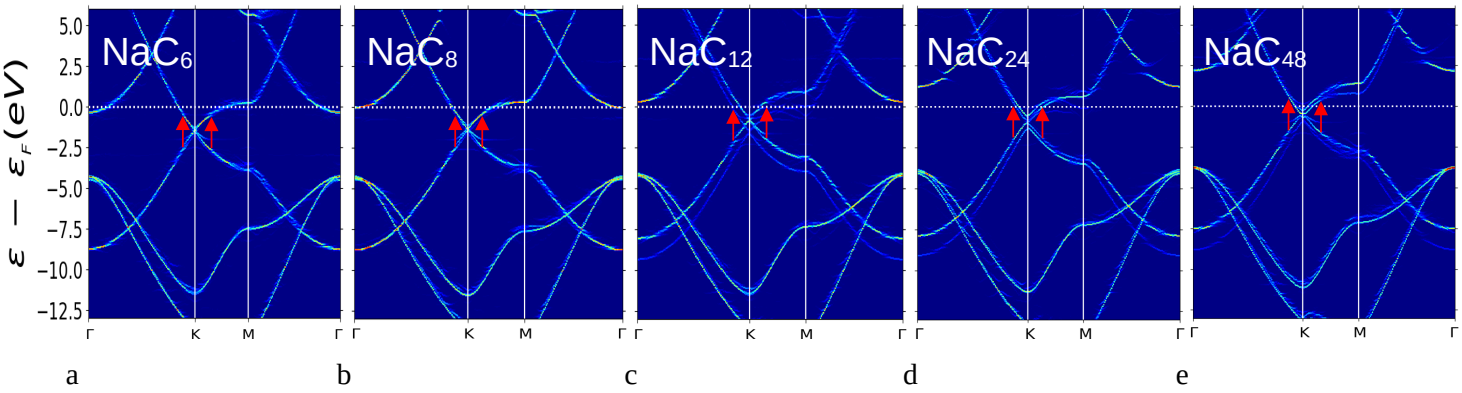

Fig. 11 : Electronic band structure of MV defect back-folded to the Brillouin zone of graphite for Na ions regarding different stoichiometry. The red arrows in the vicinity of the K-point in reciprocal space, corresponding to the typical excitation energy of a laser applied in Raman experiments, having a wavelength of 633 nm (1.96 eV).

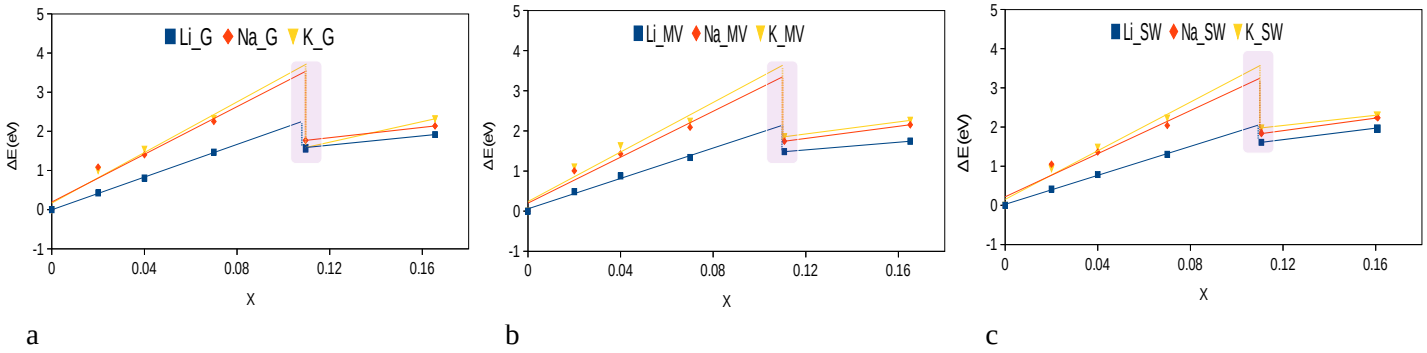

Fig. 12 : Fermi-energy shift for different stoichiometry regarding (a) pristine graphite, (b) MV, and (b) SW defects, (X corresponds to the number of ions divided by the total number of atoms)

that show different layer spacings e.g. corrsponding to those of a KC_{12} intercalation compound (see Fig. 5 in the SI). In principle, this splitting is a consequence of a lowering in symmetry. This also explains why it is observed for AB stacked graphite but not for its AA stacked analogon (see Fig. S6 in the SI).

4 Conclusions

In conclusion, we used first-principles calculations to investigate the intercalation of Li, Na, and K in defect-containing, graphite based model systems to mimic the intercalation process in hard carbon anodes. According to our results, the presence of defects promotes the stability of ion intercalation, in particular when unsaturated carbon bonds are present. Thus, defects in principle can increase the capacity of interlayer storage in carbon based materials. However, parts of this additional capacity, in particular alkali metal ions at the defect centers, may be responsible for the experimentally observed irreversible capacity losses during the first charge. On the other hand, additional interlayer sites are also created at low potentials and these, together with an increased layer spacing, are important for allowing a fast diffusion of AM ions to micro- and nano-pores. These insights might be used for the rational design of hard carbon based anode materials with improved properties.

Finally, we demonstrated that the intercalation process in pristine and defective graphite results in a similar change in the vibrational spectrum, most prominently in the shift of the G-band vibrations towards lower frequencies. Thus, in agreement with earlier studies, a shifting G-band can clearly be linked to the intercalation process in the graphitic domains, whereas a constant G-band position during discharge/charge means alkali metal adsorption/desorption in micro- and nano-pores of hard carbon anodes. Finally, the occurence of the D-band with respect to the alkali metal content has been discussed, showing that defect concentrations in the order of almost 1% do not siginificantly alter the band structure.

Conflicts of interest

There are no conflicts to declare.

Acknowledgements

This work was funded by the Deutsche Forschungsgemeinschaft (DFG, German Research Foundation) under Project ID

390874152 (POLiS Cluster of Excellence, EXC 2154). The authors acknowledge further support by the state of Baden-Württemberg through bwHPC and the German Research Foundation (DFG) through grant no INST 40/575-1 FUGG (JUSTUS 2 cluster) and by the HoreKa supercomputer funded by the Ministry of Science, Research and the Arts Baden-Württemberg and by the Federal Ministry of Education and Research. This work contributes to the research performed at CELEST (Center for Electrochemical Energy Storage Ulm-Karlsruhe).

References

1 M. Broussely, ECS Meeting Abstracts, 2007, p. 663.

2 L. He, W. Xu, Y. Song, Y. Luo, X. Liu and Z. Zhao, Global Challenges, 2018, **2**, 1700079.

3 M. Rahimi, Lithium-ion batteries: Latest advances and prospects, 2021.

4 Y. Yue and H. Liang, Small Methods, 2018, **2**, 1800056.

5 C. Gauckler, M. Dillenz, F. Maroni, L. F. Pfeiffer, J. Biskupek, M. Sotoudeh, Q. Fu, U. Kaiser, S. Dsoke, H. Euchner, P. Axmann, M. Wohlfahrt-Mehrens, A. Groß and M. Marinaro, ACS Appl. Energy Mater., 2022, **5**, 13735–13750.

6 H. Onuma, K. Kubota, S. Muratsubaki, W. Ota, M. Shishkin, H. Sato, K. Yamashita, S. Yasuno and S. Komaba, Journal of Materials Chemistry A, 2021, **9**, 11187–11200.

7 A. V. Desai, R. E. Morris and A. R. Armstrong, ChemSusChem, 2020, **13**, 4866–4884.

8 D. Stottmeister and A. Groß, Batteries Supercaps, 2023, **6**, e202300156.

9 O. Lenchuk, P. Adelhelm and D. Mollenhauer, Physical Chemistry Chemical Physics, 2019, **21**, 19378–19390.

10 J. Zhang, Y. Li, L. Zhu, X. Wang and J. Tu, Energy Storage Materials, 2021, **41**, 606–613.

11 J. Xu, Y. Dou, Z. Wei, J. Ma, Y. Deng, Y. Li, H. Liu and S. Dou, Advanced Science, 2017, **4**, 1700146.

12 T. Yamamoto, A. Yadav and T. Nohira, Journal of The Electrochemical Society, 2022, **169**, 050507.

13 L. Li, L. Liu, Z. Hu, Y. Lu, Q. Liu, S. Jin, Q. Zhang, S. Zhao and S.-L. Chou, Angewandte Chemie International Edition, 2020, **59**, 12917–12924.

14 Z. Jian, W. Luo, Z. Xing, C. Bommier, Z. Li and X. Ji, Electrochemical Society Meeting Abstracts imlb2016, 2016, pp. 821–821.

15 J. Zhao, X. Zou, Y. Zhu, Y. Xu and C. Wang, Advanced Functional Materials, 2016, **26**, 8103–8110.

16 Y. Liu, B. V. Merinov and W. A. Goddard III, Proceedings of the National Academy of Sciences, 2016, **113**, 3735–3739.

17 M. Khosravi, N. Bashirpour and F. Nematpour, Advanced Materials Research, 2014, **829**, 922–926.

18 X. Zhang, S. Han, P. Xiao, C. Fan and W. Zhang, Carbon, 2016, **100**, 600–607.

19 S. M. Jafari, M. Khosravi and M. Mollazadeh, Electrochimica Acta, 2016, **203**, 9–20.

20 H. Yu, X. Dong, Y. Pang, Y. Wang and Y. Xia, Electrochimica Acta, 2017, **228**, 251–258.

21 I. Zsoldos, Nanotechnology, Science and Applications, 2010, 101–106.

22 H. Zheng, Q. Qu, L. Zhang, G. Liu and V. S. Battaglia, RSC advances, 2012, **2**, 4904–4912.

23 M. Drews, J. Büttner, M. Bauer, J. Ahmed, R. Sahu, C. Scheu, S. Vierrath, A. Fischer and D. Biro, ChemElectroChem, 2021, **8**, 4750–4761.

24 M. Thompson, Q. Xia, Z. Hu and X. S. Zhao, Materials Advances, 2021, **2**, 5881–5905.

25 A. Kamiyama, K. Kubota, T. Nakano, S. Fujimura, S. Shiraishi, H. Tsukada and S. Komaba, ACS Applied Energy Materials, 2019, **3**, 135–140.

26 H. Yamamoto, S. Muratsubaki, K. Kubota, M. Fukunishi, H. Watanabe, J. Kim and S. Komaba, Journal of Materials Chemistry A, 2018, **6**, 16844–16848.

27 Z. Jian, Z. Xing, C. Bommier, Z. Li and X. Ji, Advanced Energy Materials, 2016, **6**, 1501874.

28 A. Kamiyama, K. Kubota, T. Nakano, S. Fujimura, S. Shiraishi, H. Tsukada and S. Komaba, ACS Applied Energy Materials, 2019, **3**, 135–140.

29 E. Buiel, A. George and J. Dahn, Carbon, 1999, **37**, 1399–1407.

30 J. Dahn, W. Xing and Y. Gao, Carbon, 1997, **35**, 825–830.

31 M. Anji Reddy, M. Helen, A. Groß, M. Fichtner and H. Euchner, ACS Energy Letters, 2018, **3**, 2851–2857.

32 H. Euchner, B. P. Vinayan, M. A. Reddy, M. Fichtner and A. Groß, Journal of Materials Chemistry A, 2020, **8**, 14205–14213.

33 B. Xiao, T. Rojo and X. Li, ChemSusChem, 2019, **12**, 133–144.

34 A. A. Arie, H. Kristianto and H. Muljana, Electrochemical Society Meeting Abstracts 236, 2019, pp. 534–534.

35 D. Ledwoch, D. J. Brett and E. Kendrick, ECS Transactions, 2016, **72**, 17.

36 A. Baranov, Y. S. Bobovich and V. Petrov, Journal of Raman spectroscopy, 1993, **24**, 695–697.

37 C. Thomsen and S. Reich, Physical review letters, 2000, **85**, 5214.

38 T. Dines, D. Tither, A. Dehbi and A. Matthews, Carbon, 1991, **29**, 225–231.

39 H. Jalili, B. Aslibeiki, A. Hajalilou, O. Musalu, L. Ferreira and M. Cruz, Ceramics International, 2022, **48**, 4886–4896.

40 M. Drews, J. Büttner, M. Bauer, J. Ahmed, R. Sahu, C. Scheu, S. Vierrath, A. Fischer and D. Biro, ChemElectroChem, 2021, **8**, 4750–4761.

41 Z. Li, C. Bommier, Z. Chong, Z. Jian, T. Surta, X. Wang, Z. Xing, J. Neuefeind, W. Stickle, M. Dolgos et al., Adv. Energy Chem., 2017, **7**, 1602894–1602903.

42 A. Vasileiadis, Y. Li, Y. Lu, Y.-S. Hu and M. Wagemaker, ACS Applied Energy Materials, 2022, **6**, 127–140.

43 Z. Zhao, H. Chen, W. Zhang, S. Yi, H. Chen, Z. Su, B. Niu, Y. Zhang and D. Long, Materials Advances, 2023.

44 G. Kresse and J. Furthmüller, Physical review B, 1996, **54**, 11169.

45 G. Kresse and D. Joubert, Physical review b, 1999, **59**, 1758.

46 G. Kresse and J. Furthmüller, Computational materials science, 1996, **6**, 15–50.
47 A. Togo and I. Tanaka, Scripta Materialia, 2015, **108**, 1–5.
48 P. V. Medeiros, S. Stafström and J. Björk, Physical Review B, 2014, **89**, 041407.
49 P. V. Medeiros, S. S. Tsirkin, S. Stafström and J. Björk, Physical Review B, 2015, **91**, 041116.
50 F. Zheng and P. Zhang, Computer Physics Communications, 2017, **210**, 139–144.
51 L. Li, S. Reich and J. Robertson, Physical Review B, 2005, **72**, 184109.
52 P.-c. Tsai, S.-C. Chung, S.-k. Lin and A. Yamada, Journal of Materials Chemistry A, 2015, **3**, 9763–9768.
53 I. A. Pašti, A. Jovanović, A. S. Dobrota, S. V. Mentus, B. Johansson and N. V. Skorodumova, Physical Chemistry Chemical Physics, 2018, **20**, 858–865.
54 M. Heggie, G. Haffenden, C. Latham and T. Trevethan, Philosophical Transactions of the Royal Society A: Mathematical, Physical and Engineering Sciences, 2016, **374**, 20150317.
55 F. L. Thiemann, P. Rowe, A. Zen, E. A. Muller and A. Michaelides, Nano Letters, 2021, **21**, 8143–8150.
56 C. Tayran, S. Aydin, M. Cakmak and Ş. Ellialtıoğlu, Solid State Communications, 2016, **231**, 57–63.
57 H. Euchner and A. Groß, Physical Review Materials, 2022, **6**, 040302.
58 N. Yoshinari and T. Konno, Chemistry Letters, 2021, **50**, 697–710.